Absorption and emission spectroscopy of matrix-isolated benzo[g,h,i]perylene: An experimental and theoretical study for astrochemical applications

Xavier Chillier
*Space Science Division, M/S 245-6, NASA-Ames Research Center, Moffett Field, California 94035-1000
and Département de Chimie Physique, Université de Genève, 30 quai E-Ansermet,
CH-1211 Genève 4, Switzerland*

Pascal Boulet
*Département de Chimie Physique, Université de Genève, 30 quai E-Ansermet, CH-1211 Genève 4,
Switzerland, and Laboratoire de Chimie Physique Théorique, Université Claude Bernard Lyon 1, Bât. 210,
43 bd du 11 Novembre 1918, F-69622 Villeurbanne Cedex et Institut de Recherche sur la Catalyse,
UPR 5401, F-69626 Villeurbanne Cedex, France*

Henry Chermette
*Laboratoire de Chimie Physique Théorique, Université Claude Bernard Lyon 1, Bât. 210,
43 bd du 11 Novembre 1918, F-69622 Villeurbanne Cedex et Institut de Recherche sur la Catalyse,
UPR 5401, F-69626 Villeurbanne Cedex, France*

Farid Salama
Space Science Division, M/S 245-6, NASA-Ames Research Center, Moffett Field, California 94035-1000

Jacques Weber
*Département de Chimie Physique, Université de Genève, 30 quai E-Ansermet,
CH-1211 Genève 4, Switzerland*

The absorption and emission spectra of benzo[g,h,i]perylene, a six ring polycyclic aromatic hydrocarbon molecule ($C_{22}H_{12}$), embedded in a rare gas matrix are reported. Time dependent emission shows that this molecule exhibits sharp phosphorescence in the red. Supporting theoretical calculations using the recently developed time-dependent density-functional response theory formalism (TD–DFRT) allow a tentative assignment for the observed transitions. The astrochemical significance of the results is briefly discussed. © *2001 American Institute of Physics.*
[DOI: 10.1063/1.1376632]

I. INTRODUCTION

Spectroscopic studies of polycyclic aromatic hydrocarbons (PAHs) are required to test the validity of the PAH hypothesis.[1] This hypothesis in its ambitious form[2] implies that PAHs are an important reservoir of carbon in the universe[3-5] (~2% up to 20% of the total carbon budget) and that they are responsible for (i) the unidentified infrared emission bands (UIRs) in the mid-IR range (~3000–800 cm^{-1}) and (ii) some of the diffuse interstellar bands (DIBs), broad absorption bands extending from the UV through to the NIR which are associated with the diffuse interstellar medium.

Several physico-chemical constraints are implied in the PAH model: the class of molecules that carries the observed interstellar absorption and emission signals must be photostable up to roughly 10 eV (Ref. 6) and readily synthesized under specific circumstellar conditions. Astrophysical observations which support the PAH model include the facts that the UIRs and DIBs are observed in carbon rich objects and disappear in the H-II regions such as the Trapezium in Orion where the energy and the flux of photons overwhelm even species as stable as PAHs.[7]

Although open questions remain, the PAH model is now gaining acceptance. Other evidence that is consistent with the widespread distribution of PAHs includes the facts that (i) PAHs are found in carbonaceous meteorites, Antarctica micro-meteorites,[8] interstellar grains,[9] and interplanetary dust particles;[10] (ii) the IR spectrum of a typical PAH mixture ($C_{10} \rightarrow C_{48}$, neutral and cationic species) matches well the mid-IR interstellar emission;[11] (iii) several PAHs and/or PAH ions have their absorption bands close to the position of the DIBs when interstellar conditions are approximated in the laboratory using Ne matrices.[12-14] These promising results open now the way for jet experiments in the gas phase,[15,16] (iv) it has recently been shown that the matrix-isolated PAH cation, perylene$^+$, fluoresces in the visible when excited in the UV[17,18] and, finally, (v) recent astronomical observations, connecting some DIBs and the red emissions, support the hypothesis of a unique class of carriers responsible for the interstellar absorption and emission bands.[19]

Furthermore, PAHs are a class of remarkably photostable organic molecules that are readily formed in carbon-rich environments such as those found in C-rich circumstellar shells. Although the origin of interstellar PAHs is unknown, various mechanisms exist in space that could ac-

count for the formation of PAHs. The potential interstellar synthesis routes include (i) ion–molecule reactions or organometallic catalysis[20] (acetylene condensation) in the gas phase in cold molecular clouds; (ii) surface catalysis on interstellar grains; (iii) photochemical processes[21] in interstellar ices (CO/H_2O); and (iv) synthesis during the ejection phase of a Red Giant.[22]

Completing the picture of the photophysics of interstellar PAHs, we show that some neutral PAHs exhibit sharp phosphorescence bands that may contribute to the red emissions. To analyze this possible contribution to the interstellar emission we use benzo[g,h,i]perylene as a test case. First, interstellar conditions are simulated in the laboratory using the matrix isolation spectroscopy (MIS) technique to record the absorption and emission spectra of benzo[g,h,i]perylene ($C_{22}H_{12}$). Second, using theoretical calculations performed with the recently developed time-dependent density-functional response theory formalism (TD–DFRT), we tentatively assign the observed transitions.

II. EXPERIMENT

A. Matrix isolation technique

The cryogenic sample chamber, the optical system and the spectral light sources have been described elsewhere.[13,18] The cubic sample chamber is part of a stainless-steel, ultra-high vacuum system containing four large ports located at 90° with respect to one another and two gas injection inlets at 45° angles with respect to the ports. The cryogenic sample holder, suspended in the center of the chamber, accommodates a 20×1 mm sapphire window that is rotatable through 360°. An ultra-high vacuum ($p < 2.10^{-8}$ T) was continuously maintained with a combination of diffusion and mechanical pumps. The pressure was monitored with ion (CVC GIC-048-2) and thermocouple (CVC GTC-036) gauges mounted on the manifold. For Ar matrix experiments, the sapphire substrate was cooled down to 10 K using a closed-cycle cryostat (APD Cryogenics, Inc. model HC-2). The temperature was monitored with a pair of Fe–Au/Chromel thermocouples (Scientific Instruments model 9650 digital T controller) mounted on the window holder and at the cold tip of the cryostat, respectively.

The setup is only slightly modified for neon matrix experiments.[13] In this case, the substrate is cooled down to 4.2 K using a variable temperature liquid helium transfer cryostat (High Tran Refrigerator, Hansen Associates HLT-183). The temperature of the substrate is controlled by regulating the flow of liquid helium through a needle valve mounted at the end of the transfer line. A resistive heater operated by a program controller (Hansen Associates Series 8000) also allows to automatically bring the sample holder from the lowest temperature (4.2 K) to room temperature.

The two ports along the main optical axis are equipped with quartz windows and were used to record the absorption spectra. Luminescence spectra were pumped through the spectroscopy port mounted at 90° with respect to the main optical axis and equipped with a MgF_2 vacuum window. The cold sapphire window was rotated to ~45° with respect to the exciting light beam for the emission measurements. The

PAH deposition furnace was mounted on the fourth port.

Absorption spectra were recorded from 200 to 500 nm using a 600 line/mm grating blazed at 400 nm, while the luminescence spectra spanning the range from 400 to 900 nm were measured with a 200 line/mm grating blazed at 1000 nm. The light from the chamber was collected and focused on the entrance slit with two fused silica glass lenses (diam.=4 cm, f.l.=5 cm), placed 10 cm away from the sample. The signal was integrated over 25–100 scans at a typical exposure time of 0.1 s per scan for absorption and 1 s for emission experiments. This setup provided a typical resolution of 0.1 nm for absorption and 0.3 nm for emission. For time resolved experiments, the spectrometer was setup to record and store a single scan with an approximate repetition rate of 0.3 s. The exposure time was optimized at 0.3 s to improve the S/N ratio. Neon matrix absorption spectra were measured at 4.2 K with a very similar setup described in Ref. 13.

The sample preparation is standard. Briefly, once the sapphire window was at 10 K (respectively, at 4.2 K for Ne deposition), Ar deposition was started at a rate of ~10 mmole/h. Typically, argon/benzo[g,h,i]perylene ratios of approximately 2000 were achieved in this manner. The overall procedure consisted in (i) depositing the neutral sample (~1 hour deposition) and (ii) recording absorption spectra to monitor the degree of isolation of benzo[g,h,i]perylene in the matrix and to optimize the deposition rate. This was followed by the measurement of the luminescence signal(s).

B. Theoretical calculations

Theoretical work has been undertaken using density-functional theory[23] utilizing the Kohn–Sham[24] approach as implemented in the ADF package.[25] The Becke's exchange functional[26] (B88) and Perdew's correlation functional[27] (P86) have been used to optimize the benzo[g,h,i]perylene's geometrical parameters. The basis sets used are a combination of three Slater-type orbitals (triple zeta), with a polarization function added on both C and H atoms.

Calculations of the photophysical properties of benzo[g,h,i]perylene have been performed within the time-dependent density-functional response theory (TD–DFRT) formalism[28–30] using the relaxed geometry of benzo[g,h,i]perylene obtained from a generalized gradient approximation (GGA) calculation (B88[26] exchange functional and P86[27] correlation functional).

For the absorption spectra, the ground state geometry of benzo[g,h,i]perylene has been used whereas for the fluorescence and phosphorescence, the geometry optimized for both the first singlet and the first triplet excited states have been used, respectively. It is worthwhile to mention that for both singlet and triplet excited states the symmetry of the ground state has been retained (C_{2v}). However, a test calculation has shown that the geometry does not change significantly from C_{2v} to C_1 during this transition. Finally, for the theoretical vibronic analysis, the vibrational spectrum of the first singlet excited state of benzo[g,h,i]perylene has been used for the absorption spectra, whereas that of the ground state has been used for the fluorescence and phosphorescence spectra.
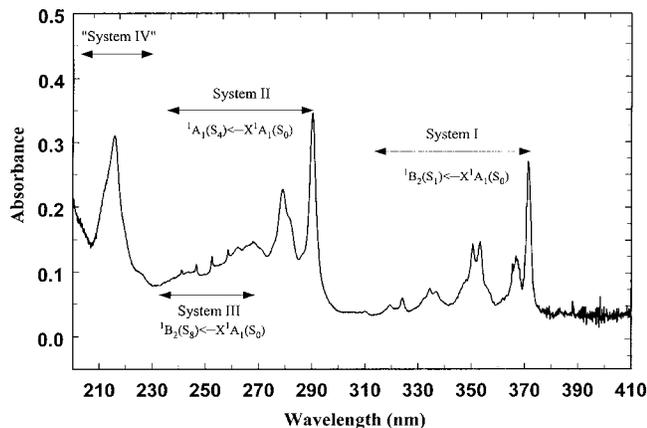
FIG. 1. Absorption spectrum of benzo[g,h,i]perylene isolated in a Ne matrix at 5 K.

III. RESULTS AND DISCUSSION

A. Absorption spectroscopy

The absorption spectrum of benzo[g,h,i]perylene embedded in a neon matrix[31] is shown in Fig. 1. Measurements were taken in the 200–900 nm range. The first observed band emerges at about 372 nm while other bands peak at higher frequencies up to 200 nm (the experimental limit). The absorption spectrum of benzo[g,h,i]perylene can be divided into three distinct band systems with more or less similar apparent intensity. The longest wavelength system, or System I, is intense. The strongest band of this system falls at 371.5 ± 0.1 nm and shows some vibronic structure up to 310 nm. From our theoretical calculations, reported in Table I, the pure electronic (0–0) transition is assigned at 430.5 nm and corresponds to a transition from the ground electronic state to the first singlet excited state $\{^1B_2(S_1)\leftarrow X\,^1A_1(S_0)\}$.

The difference in energy observed between experiment and theory for this transition lies thus around 3700 cm^{-1}, a value in agreement with previous studies.[32–34] This transition is allowed by symmetry as the μ_y component of the electric dipolar momentum belongs to the B_2 irreducible representation. The orientation of the axes is depicted in scheme 1.
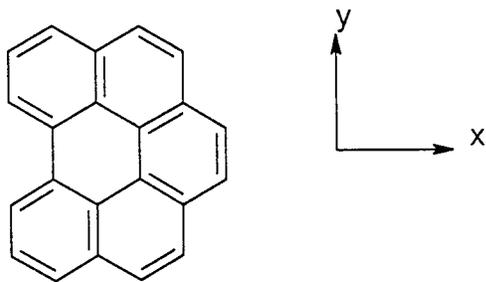
Scheme 1. Benzo[g,h,i]perylene (C_{2v}). Orientation of the axes adopted in the theoretical calculations.

As the two other components μ_x and μ_z of the dipole momentum have, respectively, B_1 and A_1 symmetries, the vibronic transitions allowed by the selection rules stem from the A_2, B_2, and A_1 irreducible representations. The main vibronic transitions emerge at 366.9 nm ($\Delta\nu_{[0-1]}$

$=335$ cm^{-1}), 353 nm ($\Delta\nu_{[0-2]}=1447$ cm^{-1}), 351 nm ($\Delta\nu_{[0-3]}=1508$ cm^{-1}), 337 nm ($\Delta\nu_{[0-4]}=2792$ cm^{-1}), 334.6 nm ($\Delta\nu_{[0-5]}=3004$ cm^{-1}), 334.2 nm ($\Delta\nu_{[0-6]}=3967$ cm^{-1}), and 319.5 nm ($\Delta\nu_{[0-7]}=4418$ cm^{-1}). Table I presents a tentative assignment for these transitions. Vibrations with a B_1-symmetry wave function are not allowed by symmetry to contribute to the $S_1\leftarrow S_0$ transition. For this system, the three main active vibrations are 1508, 1447, and 335 cm^{-1} with A_1, A_1, and B_2 symmetries, respectively. The anharmonicity of the oscillator can be estimated for the 1508 cm^{-1} vibrational quantum. The anharmonicity constant $\omega_e x_e$ amounts to 6 cm^{-1} which leads to $x_e=0.004$. The first overtone is calculated at 3004 cm^{-1} $\{2\omega_e-6\omega_e x_e=2*1508-12\}$, while the second overtone is calculated at 4488 cm^{-1} $\{3\omega_e-12\omega_e x_e=3*1508-36\}$. The calculated vibrational intensities in km mole^{-1} (see Table I) must be taken with care as the vibrations observed in the spectra are vibronic transitions and not pure vibrations. Some of the vibrations can appear weak or null from the calculations whereas they can be active and intense in the experimental spectrum.

System II absorbs to the blue of System I with its strongest transition peaking at 290.6 ± 0.1 nm. System II exhibits a unique vibronic band at 279.5 ± 0.1 nm although some of the band structure may be embedded in the next, overlapping, band system. According to the theoretical calculations, the pure electronic (0–0) transition lies around 338.8 nm (29 512 cm^{-1}) and is associated to the transition from the ground electronic state to the fourth singlet excited state $\{^1A_1(S_4)\leftarrow X\,^1A_1(S_0)\}$. This transition is symmetry allowed. According to our assignments, the difference in energy between calculated and observed transitions amounts to about 5000 cm^{-1}. This transition is allowed by symmetry, the μ_z component of the electric dipolar momentum belonging to the A_1 irreducible representation. For the vibronic transitions, the allowed symmetries of the vibrational wave function for this electronic state are A_1, B_1 and B_2. The vibronic transition emerges at $\Delta\nu_{[0-0]}=1367$ cm^{-1} and matches fairly well with the calculated vibrations of the A_1-symmetry band located at $\Delta\nu_{[0-0]}=1332$ cm^{-1}.

The vibronic transitions observed in Systems I and II are very characteristic of PAH molecules. Spacings in the range 1600–1200 cm^{-1} are typically associated in these molecules with aromatic C–C stretching bands and some combination bands involving C–H in-plane bending modes.

The onset of absorption of System III overlaps with System II. Theoretical calculations can help guide band assignment. Considering (i) that the pure electronic (0–0) transition corresponding to the transition from the ground state to the eighth singlet excited state $\{^1B_2(S_8)\leftarrow X\,^1A_1(S_0)\}$ is calculated at 304.7 nm (32 820 cm^{-1}) and (ii) that the shift between the observed and the calculated values of the 0–0 transition of System III is similar to that observed for Systems I and II, i.e., of the order of 3500–5000 cm^{-1}, it results that the 0–0 transition of System III should be shifted by about 4500 cm^{-1} to the blue of System II. Figure 1 shows indeed a peak at 268 nm (37 313 cm^{-1}) that is assigned to the 0–0 transition of $^1B_2(S_8)\leftarrow X\,^1A_1(S_0)$. System III exhibits a rich vibronic structure as shown in Table I. The most

TABLE I. Absorption spectrum of benzo[g,h,i]perylene.

			Experiment					Theoretical calculations			
			Anharmonicity				Oscillator			Absorption intensity	
λ (nm)	ν (cm^{-1})	$\Delta\nu^{exp}$ (cm^{-1})	$\omega_e x_e$ (cm^{-1})	x_e	Overtones or linear combination	ν (cm^{-1})	strength (a.u.)	ω_e (cm^{-1})	Symmetry	(km mol^{-1})	Description[a]
System I $^1B_2(S_1)\leftarrow X\,^1A_1(S_0)$											
371.45	26 922	0				23 232	0.17				
366.88	27 257	335						394	B_2	11	Rocking
353.00	28 329	1447						1447	B_2	0.5	$\epsilon_{CC}+\delta_{CCH}$ (in plane)
351.00	28 390	1508	6	0.004	$\omega_e-2\omega_e x_e=1508$			1518	A_1	21	$\epsilon_{CC}+\delta_{CCH}$ (in plane)
337.00	29 674	2792			$4*335+1447=2787$						
334.60	29 886	3004	6	0.004	$2\omega_e-6\omega_e x_e=3004$						
324.16	30 849	3967			$3*335+1447+1508=3960$						
319.49	31 300	4418	6	0.004	$3\omega_e-12\omega_e x_e=4488$						
System II $^1A_1(S_4)\leftarrow X\,^1A_1(S_0)$											
290.60	34 411	0				29 512	0.22				
279.50	35 778	1367						1332	A_1	13	$\epsilon_{CC}+\delta_{CCH}$ (in plane)
System III $^1B_2(S_8)\leftarrow X\,^1A_1(S_0)$											
268.00	37 313	0				32 820	0.18				
262.00	38 168	855						825	A_2	0	δ_{CCC} (out of plane)
258.00	38 760	1447						1447	B_2	0.5	$\epsilon_{CC}+\delta_{CCH}$ (in plane)
252.50	39 604	2291			$855+1447=2302$						
247.00	40 486	3173			$2*855+1447=3157$						
242.00	41 322	4009			$3*855+1447=4012$						
"System IV" $14\,^1A_1\leftarrow X\,^1A_1(S_0)$, $15\,^1B_2\leftarrow X\,^1A_1(S_0)$, $15\,^1A_1\leftarrow X\,^1A_1(S_0)$, $16\,^1A_1\leftarrow X\,^1A_1(S_0)$, $17\,^1A_1\leftarrow X\,^1A_1(S_0)$											
222.00	44 248	0				45 411	0.42				
216.00	46 296	0				46 472	1.41				
214.00	46 729	0				48 639	0.12				
						49 337	0.65				
						50 565	0.43				

[a]δ and ϵ correspond to bending and stretching modes, respectively.

active vibrations are $\Delta\nu_{[0-0]}=1447$ and 855 cm^{-1}. These values are typically associated with aromatic C–H in-plane bending modes and/or aromatic C–C stretching modes for the first one and with aromatic out-plane C–H bending modes for the second one. Because the symmetry of the electronic wave function is B_2, the symmetry of the vibrational wave function should be A_1, A_2 or B_2 (B_1 is allowed as it has been previously mentioned).

Finally, "System IV" appears as a broad, nonresolved, peak around 216 nm with a FWHM of approximately 2165 cm^{-1}. Potential saturation effects as well as overlap on the short wavelength side ($\lambda\leqslant200$ nm) with the very strong Schumann–Runge system of atmospheric O$_2$ ($\Sigma_u^-\leftarrow X\Sigma_g^-$) contribute to obscuring the vibronic structure. Nevertheless, theory predicts various strong and very strong transitions in this region of the spectrum: $14\,^1A_1\leftarrow X\,^1A_1(S_0)$ at 220.2 nm (45 411 cm^{-1}), $15\,^1B_2\leftarrow X\,^1A_1(S_0)$ at 215.2 nm (46 472 cm^{-1}), $15\,^1A_1\leftarrow X\,^1A_1(S_0)$ at 205.6 nm (48 639 cm^{-1}), $16\,^1A_1\leftarrow X\,^1A_1(S_0)$ at 202.7 nm (49 337 cm^{-1}), and $17\,^1A_1\leftarrow X\,^1A_1(S_0)$ at 197.8 nm (50 565 cm^{-1}). System IV might be composed of an overlap of some of these electronic transitions.

B. Emission spectroscopy

When excited at 375 ± 20 nm (i.e., in System I), benzo[g,h,i]perylene isolated in an argon matrix exhibits a

rich structured emission spectrum in the 400 to 520 nm range (Fig. 2). The emission bands frequencies and relative intensities do not change when the pumping excitation is scanned through the UV range. It is also interesting to note the presence of fine structure above 600 nm (Fig. 2) which appears to belong to another, weaker, emission band system. A crude time resolved experiment shows that these signals persist after the excitation cutoff. Figure 3 shows that the signals above 600 nm are detectable for approximately ~1 second
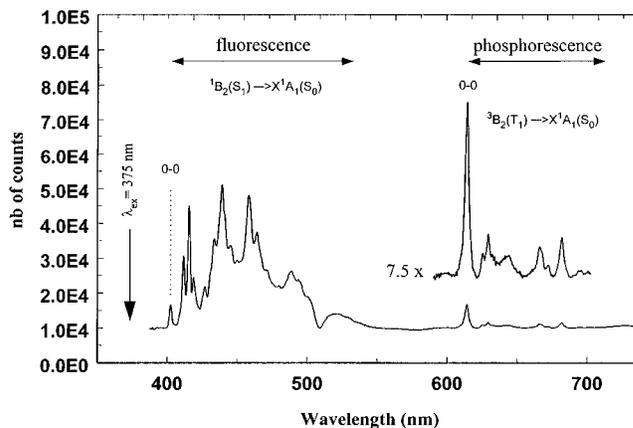
FIG. 2. Emission spectra of benzo[g,h,i]perylene isolated in an Ar matrix at 10 K.
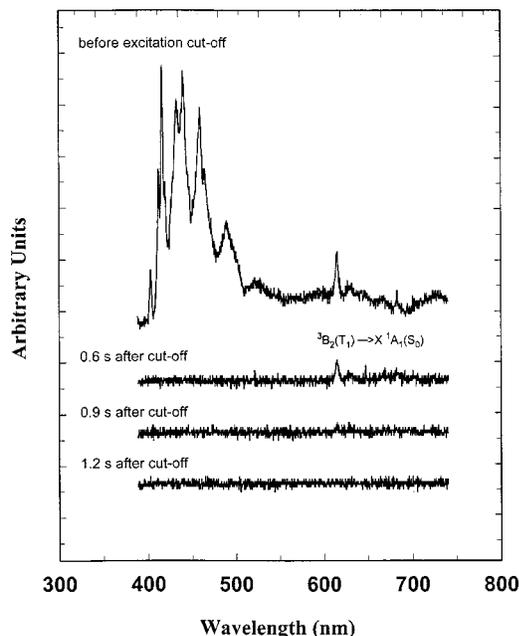
FIG. 3. Time resolved experiment of the phosphorescence spectrum of benzo[g,h,i]perylene isolated in an Ar matrix at 10 K.

after the excitation cutoff, whereas the signals on the blue side of the spectrum ($\lambda < 520$ nm) disappear instantaneously. Because phosphorescence is a slow relaxation process, the signals above 600 nm are thought to be due to phosphorescence, whereas the signals below 520 nm should correspond to fluorescence. In Fig. 3, a weak signal seen at 520 nm (19 230 cm^{-1}) seems to persist for 0.6 s. This signal may be due to the transition from the second triplet state to the ground electronic state but it is too weak to be conclusively assigned. Note that theory predicts the second triplet state T_2 ($^3A_1$) to be located at 520 nm. Consequently, the emission spectrum of benzo[g,h,i]perylene can be divided into two emission band systems as follows. System I, fluorescence from the first excited singlet state; System II, phosphorescence from the first excited triplet state.

System I: The difference in energy between the pure electronic (0–0) transition of benzo[g,h,i]perylene in the absorption mode and in the emission mode amounts to about 1481 cm^{-1}. This value denotes a substantial change in geometry between the first excited singlet state and the ground electronic state of the molecule when isolated in an argon cage. According to theoretical calculations, the RMS (root mean square) deviation between the CC bonds in the ground and the excited states amounts to 0.020 Å. The RMS on CH bonds is smaller (0.0007 Å). Theoretical calculations predict the pure electronic transition from the first excited singlet state to the ground electronic state $\{^1B_2(S_1) \rightarrow X\,^1A_1(S_0)\}$ at 465.6 nm (21 748 cm^{-1}).

This transition is observed at 402.7 nm (24 833 cm^{-1}) in our experiments (Fig. 2). From a theoretical point of view, this blueshift of about 3300 cm^{-1} is satisfactory as explained in the following section.

The vibronic structure of the emission system is rich and the bands are more intense than the 0–0 transition. This phenomenon is generally associated with the difference of ge-

ometry between the excited and the ground states. The larger the difference of geometry between the two states, the larger the intensity of the vibronic transitions compared to the 0–0 band. In other words, the 0–0 transition becomes marginal when the ground state and the excited state geometries differ greatly.

Because the symmetry of the upper electronic state is B_2, the authorized symmetries for the vibrational wave functions are restricted to A_1, A_2 and B_2, B_1 being forbidden. Table II presents tentative of assignments for all the measured transitions. The most active modes are the vibrations with a quantum of $\Delta \nu_{[0-0]} = 780$, 953, and 1414 cm^{-1}. Almost all vibronic transitions of System I can be explained by linear combinations or overtones of these three modes. Although the anharmonicities of the oscillators are quite high for the vibration with a quantum of 953 cm^{-1} ($\omega_e x_e = 65$ cm^{-1}) and even larger for the one with a quantum of 1414 cm^{-1} ($\omega_e x_e = 107$ cm^{-1}), the overtones can be predicted with a remarkable precision up to the fourth ones.

System II exhibits sharp and well-resolved structures above 600 nm. Because of its relatively slow relaxation period, System II is thought to be associated with phosphorescence as discussed above. The most intense peak, assumed to be the pure electronic (0–0) transition of that system, is observed at 614.1 nm (16 283 cm^{-1}). This measurement is in good agreement with the theoretical calculations which predict the pure electronic transition between the first triplet state ($^3B_2$) and the ground electronic state $\{^3B_2(T_1) \rightarrow X\,^1A_1(S_0)\}$ at 611.7 nm (16 347 cm^{-1}). Although this transition is spin-forbidden it is clearly observed on the spectrum indicating a large spin–orbit coupling and a symmetry allowance by the spin–orbital wave function (ψ_{es}). Note that increased spin–orbit coupling is expected in a solid argon matrix. In triplet states ($S = 1$), the spin wave function (ψ_s) may influence the symmetry of the electronic wave function (ψ_{es}). Two types of couplings are then possible:[35] case (a) or case (b). In case (a), the spin–orbital wave function can be written as the product, $\psi_{es} = \psi_e \times \psi_s$. In case (b), the spin–orbital wave function (ψ_{es}) directly equals its own electronic part ψ_e ($\psi_{es} = \psi_e$).

In case (b), the pure electronic transition $^3B_2(T_1) \rightarrow X\,^1A_1(S_0)$ is symmetry allowed by the μ_y component of the dipolar momentum. Therefore, the irreducible representations of the vibrational wave functions allowed by symmetry for the vibronic transitions are the same as for the first excited singlet state $^1B_2$, i.e., $\Gamma(\psi_v) = A_2$, A_1, and B_2.

In case (a), for triplets in the C_{2v} geometry, $\Gamma(\psi_s)$ is transformed as the rotation components of this group: $R_x \in B_2$, $R_y \in B_1$, and $R_z \in A_1$. By consequence, the integral $\langle \psi''_{es} | \mu | \psi'_{es} \rangle$ shows that the three components of the electric dipolar momentum belongs to the B_1 irreducible representation. Therefore, the pure electronic $^3B_2(T_1) \rightarrow X\,^1A_1(S_0)$ transition would be forbidden in a case (a) hypothesis and only vibronic transitions with a vibrational wave function of B_1 symmetry would be allowed. Although we cannot prove this fact (in matrices, no rotational resolution can be expected and our spectral resolution is too low), the hypothesis of case (b) appears more in accordance with the aspect of the observed phosphorescence spectrum.

TABLE II. Emission spectra of benzo[g,h,i]perylene.

Experiment						Theoretical calculations					
			Anharmonicity				Oscillator			Absorption intensity	
λ (nm)	ν (cm^{-1})	$\Delta\nu^{\mathrm{exp}}$ (cm^{-1})	$\omega_e x_e$ (cm^{-1})	x_e	Overtones or linear combination	ν (cm^{-1})	strength (a.u.)	ω_e (cm^{-1})	Symmetry	(km mol^{-1})	Description[a]
					Fluorescence						
System I $^1B_2(S_1)\rightarrow X\,^1A_1(S_0)$											
402.66	24 835	0				21 478	0.17				
411.72	24 288	547						538	A_1	0.1	Breathing
415.71	24 055	780						802	B_2	1.5	δ_{CCC} (out of plane)
418.72	23 882	953	65	0.060	$\omega_e-2\omega_e x_e=953$			917	A_1	1.4	δ_{CCC} (out of plane)
425.10	23 524	1311						1324	A_1	1.2	ϵ_{CC}
426.97	23 421	1414	107	0.066	$\omega_e-2\omega_e x_e=1414$			1397	B_2	0.8	$\epsilon_{\mathrm{CC}}+\delta_{\mathrm{CCH}}$
430.64	23 221	1614						1606	A_1	2.6	$\epsilon_{\mathrm{CC}}+\delta_{\mathrm{CCH}}$
433.69	23 058	1777	65	0.060	$2\omega_e-6\omega_e x_e=1777$						
437.37	22 864	1971			$547+1414=1961$						
439.13	22 772	2063									
441.34	22 658	2177									
445.18	22 463	2372			$953+1414=2367$						
450.00	22 222	2613	107	0.066	$2\omega_e-6\omega_e x_e=2613$						
458.40	21 815	3020	65	0.060	$3\omega_e-12\omega_e x_e=3028$						
463.86	21 543	3292			$3*780+953=3293$						
471.07	21 228	3607	107	0.066	$3\omega_e-12\omega_e x_e=3603$						
480.12	20 828	4007			$780+2*1614=4008$						
488.78	20 459	4376	107	0.066	$4\omega_e-20\omega_e x_e=4376$						
493.75	20 253	4582			$4*953+780=4592$						
500.57	19 977	4858			$5*780+953=4853$						
520.64	19 207	5628			$3*1614+780=5622$						
					Phosphorescence						
System II $^3B_2(T_1)\rightarrow X\,^1A_1(S_0)$											
614	16 283	0				16 347	0				
625	15 987	296						294	A_2	0	δ_{CCC} (out of plane)
629	15 886	397						405	B_2	4	Rocking
643	15 543	740						757	A_2	0	δ_{CCH} (out of plane)
666	15 008	1275						1289	A_1	3	$\epsilon_{\mathrm{CC}}+\delta_{\mathrm{CCH}}$ (in plane)
672	14 868	1415						1407	B_2	1	$\epsilon_{\mathrm{CC}}+\delta_{\mathrm{CCH}}$ (in plane)
682	14 665	1618						1614	B_2	0.1	$\epsilon_{\mathrm{CC}}+\delta_{\mathrm{CCH}}$ (in plane)

[a]δ and ϵ correspond to bending and stretching modes, respectively.

C. Further insight on luminescent processes by computational calculations

Absorption: The absorption spectrum calculated by TD–DFRFT is presented in Table III. Three intense bands are located at 23 232, 29 512, and 32 820 cm^{-1} and correspond to the first, fourth, and eighth singlet excited states (S_1, S_4, and S_8), respectively. The $\{^1B_2(S_1)\leftarrow X\,^1A_1(S_0)\}$ and $\{^1B_2(S_8)\leftarrow X\,^1A_1(S_0)\}$ transitions have quite the same intensities (0.17 and 0.19 a.u., respectively), while the $\{^1A_1(S_4)\leftarrow X\,^1A_1(S_0)\}$ transition is slightly more intense, with an oscillator strength of 0.22 a.u. The first absorption band is associated to the pure HOMO–LUMO (HOMO and LUMO stand for highest occupied molecular orbital and lowest unoccupied molecular orbital, respectively) transition (92%). At this stage of the description, it is worthwhile to note that the valence electronic configuration of benzo[g,h,i]perylene is $5b_1^2 4a_2^2 6b_1^2 5a_2^2 7b_1^0 6a_2^0 8b_1^0 9b_1^0$. All occupied molecular orbitals (MOs) are of π-bonding character whereas all unoccupied MOs are the corresponding π^*-antibonding ones. The $^1A_1$ excited state results from the combination of the HOMO–LUMO+1 and HOMO−1–LUMO transitions, both contributing to half the total excited wave function. Fi-

nally, the HOMO−1–LUMO+1 transition is the main contributor to $^1B_2(S_8)\leftarrow X\,^1A_1(S_0)$. A series of excited states arising from weaker intensity transitions are located above the eighth singlet excited state. Afterwards, five excited states ($^1A_1$, $^1B_2$, $^1A_1$, $^1A_1$, and $^1A_1$) are calculated (in bold face in Table III), lying from 45 411 to 50 565 cm^{-1} with transition intensity rising from 0.12 to 1.41 a.u.

In summary, according to the calculations, Band System I is associated with a transition to the first excited state $\{^1B_2(S_1)\leftarrow X\,^1A_1(S_0)\}$, while Band System II corresponds to a transition to the fourth excited state $\{^1A_1(S_4)\leftarrow X\,^1A_1(S_0)\}$, and Band System III to a transition to the eighth excited state $\{^1B_2(S_8)\leftarrow X\,^1A_1(S_0)\}$. Band System IV results from a combination of highly excited states (up to the 34th state).

In view of the theoretical calculations presented in Tables I and III, two possible interpretations of the experimental spectrum can be proposed. In the first scenario, the first calculated band (23 232 cm^{-1}) corresponds to the first intense experimental peak (26 922 cm^{-1} in Fig. 1). The second intense experimental band (at 34 411 cm^{-1}) is then associated with the band calculated at 29 512 cm^{-1}. This as-

TABLE III. Absorption spectrum calculated by TD–DFRT.

Symmetry	MO composition	Energy (cm^{-1})	Oscillator strength (a.u.)	%
$^1B_2$	$5a_2 \to 7b_1$	23 232	0.17	92
$^1A_1$	$5a_2 \to 6a_2$	29 512	0.22	46
	$6b_1 \to 7b_1$			39
$^1B_2$	$6b_1 \to 6a_2$	32 820	0.19	57
	$4a_2 \to 7b_1$			14
$^1A_1$	$5a_2 \to 7a_2$	35 095	0.02	33
	$5b_1 \to 7b_1$			31
	$4a_2 \to 6a_2$			23
$^1A_1$	$4b_1 \to 7b_1$	39 275	0.02	64
	$5a_2 \to 8a_2$			11
$^1A_1$	$5a_2 \to 8a_2$	40 801	0.02	42
	$5b_1 \to 8b_1$			33
$^1A_1$	$4a_2 \to 7a_2$	41 244	0.03	53
	$5b_1 \to 8b_1$			25
	$5a_2 \to 8a_2$			10
$^1B_2$	$5b_1 \to 6a_2$	41 432	0.02	30
	$6b_1 \to 7a_2$			30
	$3a_2 \to 7b_1$			13
$^1A_1$	$3a_2 \to 7a_2$	43 896	0.02	50
	$3b_1 \to 7b_1$			40
$^1A_1$	$5a_2 \to 9a_2$	44 649	0.08	52
	$3b_1 \to 7b_1$			13
	$3a_2 \to 7a_2$			11
$^1B_2$	$5b_1 \to 7a_2$	45 016	0.06	46
	$3a_2 \to 9b_1$			35
$^1A_1$	$3a_2 \to 6a_2$	45 411	0.42	19
	$5a_2 \to 8a_2$			18
	$6b_1 \to 9b_1$			13
$^1B_2$	$5a_2 \to 10b_1$	45 867	0.02	35
	$2a_2 \to 7b_1$			34
	$5b_1 \to 7a_2$			19
$^1B_2$	$4a_2 \to 9b_1$	46 472	1.41	36
	$3a_2 \to 8b_1$			31
	$3a_2 \to 9b_1$			11
$^1A_1$	$4b_1 \to 8b_1$	48 639	0.12	71
	$4a_2 \to 8a_2$			12
$^1A_1$	$2a_2 \to 6a_2$	49 337	0.65	29
	$4b_1 \to 8b_1$			10
$^1A_1$	$4b_1 \to 9b_1$	50 565	0.43	31
	$2a_2 \to 6a_2$			25

TABLE IV. Emission spectra calculated by TD–DFRT.

Symmetry	MO composition	Energy (cm^{-1})	Oscillator strength (a.u.)	%
	Fluorescence			
$^1B_2$	$5a_2 \to 7b_1$	21 478	0.17	93
$^1A_1$	$5a_2 \to 6a_2$	28 714	0.20	38
	$6b_1 \to 7b_1$			36
	$5a_2 \to 7a_2$			16
$^1B_2$	$6b_1 \to 6a_2$	32 243	0.11	57
	$3a_2 \to 7b_1$			14
	Phosphorescence			
$^3B_2$	$5a_2 \to 7b_1$	16 347	0	99
$^3A_1$	$5a_2 \to 6a_2$	21 507	0	61
	$6b_1 \to 7b_1$			38

tense band at 23 232 cm^{-1} (Table III), would not be experimentally visible. The $^1B_1$ (32 820 cm^{-1}) state would match the experimental peak located at 34 411 cm^{-1} and finally System IV (Fig. 1) would correspond to states lying from 45 411 to 50 565 cm^{-1} (Table III). Based on this line of thinking System III of Fig. 1 would not exist.

The latter argumentation is hardly conceivable both for experimental and theoretical reasons. The fact that the first absorption transition would lead to the second excited state instead of the first one implies that the former state would decay nonradiatively towards the first singlet excited state which in turn would fluoresce toward the ground state. As far as we know, such a process would be very marginal in a matrix experiment. Furthermore, from a theoretical point of view, the second interpretation implies that the calculated absorption spectrum would be blueshifted for most of the bands which would be a very unusual result. For these reasons, the first interpretation has been retained.

Emission: As for absorption, emission of light, fluorescence or phosphorescence, is a vertical process. Therefore, TD–DFT calculations have been performed using the optimized geometry of the corresponding excited states. The results of fluorescence and phosphorescence calculations are presented in Table IV. Though the optimization of the structure of the lowest triplet state in its symmetry is not a problem in DFT, the optimization of geometrical parameters of singlet states is more questionable as the wave function is a linear combination of several Slater determinants. Nevertheless, it can be seen in Table II that the theoretical emission results are in better agreement with experiments than the absorption ones.

It has been shown[38] that TD–DFT can lead to qualitatively erroneous results in the case where substantial bond stretching occurs in the excited state involved in the excitation process. Therefore, a few calculations have been performed with geometries from different excited states. It has been noticed that, whatever the excited state considered, the transition energies are not dramatically affected. As an example, for fluorescence, the use of the $6b_1 \to 10b_1$ high excited state gives the following sequence of states: $^1B_2$ (22 646 cm^{-1}), $^1A_1$ (27 806 cm^{-1}), and $^1B_2$ (31 170 cm^{-1}), which is not very different from that of Table IV. For phosphorescence, the use of the geometry of the HOMO -1 ($6b_1$)$\to$LUMO$+1$ ($6a_2$) excited state leads to the fol-

signment leads to two possibilities for the $^1B_2$ state (32 820 cm^{-1}): either it is a "fallen state"[36] that corresponds to System IV of Fig. 1 or the peak is lumped in within the vibronic transitions of System II. The problem of "fallen states" arises when exchange functional potentials do not meet the correct asymptotic tail which is the case for the local potential we used. Therefore, a calculation using the well-behaved exchange potential derived by van Leeuwen and Baerends[37] (LB94) has been performed. The results show that there is no major difference between both calculations. In particular, the 32 820 cm^{-1} state (Table III) is downshifted by about 1000 cm^{-1} while using the LB94 potential. As a consequence, we expect System III to be lumped in. This assumption is further accredited by the theoretical analysis of the vibronic transitions, which fit nicely the experimental spectra (see Table I).

The alternative interpretation is as follows: the second 29 512 cm^{-1} peak ($^1A_1$) corresponds to the first experimental one. Therefore, and for some unknown reasons, the HOMO–LUMO transition, which is the first calculated in-

lowing states: $^3B_2$ (17 751 cm^{-1}) and $^3A_1$ (20 464 cm^{-1}). The maximum deviation amounts to 2000 cm^{-1} which is within the tolerated error bars of such calculations. Our calculations suggest therefore that fluorescence and phosphorescence features are predicted at a good level of accuracy.

The astrochemical implications of the observation of red phosphorescence in the case of benzo[g,h,i]perylene is that neutral PAHs of medium size might contribute to the interstellar emission in the optical. If PAHs are indeed widespread throughout the interstellar medium, they are expected to contribute to some of the absorption and/or emission features observed in giant clouds. The point of this experiment is not to prove or disprove the presence of benzo[g,h,i]perylene in space—for that a supersonic jet experiment is needed[15,16]—but to point out the astrophysical implications resulting from the observation of PAH luminescence to explain some observations (e.g., the UV-pumped extended red emission seen in the red rectangle in which photons from the stellar source are converted by fluorescence).

IV. CONCLUSION

The spectroscopy of benzo[g,h,i]perylene ($C_{22}H_{12}$) isolated in a cold, inert-gas environment has been investigated in the laboratory by matrix isolation. Supporting theoretical calculations have been performed using the recently developed time-dependent density-functional response theory formalism (TD–DFRT). The correlation between theory and experiment is satisfying and allows the assignment of all the electronic and vibronic transitions observed in absorption and in emission modes. A particular interest is given to the phosphorescence spectrum. The astrochemical significance of red phosphorescence is also briefly discussed in the context of the interstellar PAH model because PAHs are thought to represent a significant fraction of the total carbon budget of the Universe.

[1] L. J. Allamandola, A. G. G. M. Tielens, and J. R. Barker, Astrophys. J., Suppl. **71**, 733 (1989).
[2] X. Chillier, *Habilitation à Diriger des Recherches*, Université Claude Bernard Lyon 1, HDR 12-2000.
[3] L. J. Allamandola, in *PAHs are Everywhere!, The Cosmic Dust Connection*, edited by J. M. Greenberg (Kluwer Academic, New York, 1996), pp. 81–102.
[4] Th. Henning and F. Salama, Science **282**, 2204 (1998).
[5] F. Salama, *Polycyclic Aromatic Hydrocarbons in the Interstellar Medium*: A Review, in "Solid Interstellar Matter: The ISO Revolution" Les Houches No. 11, edited by L. d'Hendecourt, C. Joblin, and A. Jones (EDP Sciences, Les Ullis, 1999), pp. 65–88.
[6] F. Salama, E. L. O. Bakes, L. J. Allamandola, and A. G. G. M. Tielens, Astrophys. J. **458**, 621 (1996).
[7] A. Léger and L. d'Hendecourt, Astrophys. J. **146**, 81 (1985).
[8] M. Maurette, X. D. F. Chillier, S. J. Gillette, S. J. Clemett, C. Engrand, G. Kurat, and R. N. Zare, Origins Life Evol. Biosphere **28**, 425 (1998).
[9] S. Messenger, R. M. Walker, X. Gao, S. Amari, S. J. Clemett, X. D. F. Chillier, and R. N. Zare, Astrophys. J. **502**, 284 (1998).
[10] S. Messenger, S. J. Clemett, L. P. Keller, K. L. Thomas, X. Fr. D. Chillier, and R. N. Zare, Meteoritics **30**, 547 (1995).
[11] L. J. Allamandola, D. M. Hudgins, and S. A. Sandford, Astrophys. J. **511**, L115 (1999).
[12] F. Salama and L. J. Allamandola, Nature (London) **358**, 42 (1992); for a review F. Salama, in *Low Temperature Molecular Spectroscopy*, edited by R. Fausto (Kluwer, New York, 1996), pp. 169–192.
[13] F. Salama and L. J. Allamandola, J. Chem. Phys. **94**, 6964 (1991); F. Salama, C. Joblin, and L. J. Allamandola, *ibid.* **101**, 10252 (1994).
[14] A. Léger, L. d'Hendecourt, and D. Défourneau, Astron. Astrophys. **293**, L-53 (1995).
[15] D. Romanini, L. Biennier, F. Salama, A. Kachanov, L. J. Allamandola, and F. Stoeckel, Chem. Phys. Lett. **303**, 165 (1999).
[16] T. Pino, N. Bourdin, and P. Bréchignac, J. Chem. Phys. **111**, 7337 (1999).
[17] C. Joblin, F. Salama, and L. Allamandola, J. Chem. Phys. **102**, 9743 (1995).
[18] X. D. F. Chillier, B. Stone, F. Salama, and L. J. Allamandola, J. Chem. Phys. **111**, 449 (1999).
[19] P. J. Sarre, J. R. Miles, and S. M. Scarrott, Science **269**, 674 (1995).
[20] I. Ristorcelli and A. Klotz, Astron. Astrophys. **317**, 962 (1997).
[21] L. J. Allamandola, S. A. Sandford, and G. J. Valero, Icarus **76**, 225 (1988).
[22] L. J. Allamandola and A. G. G. M. Tielens, Astrophys. J. **290**, L25 (1985).
[23] P. Hohenberg and W. Kohn, Phys. Rev. A **136**, 864 (1964).
[24] W. Kohn and L. J. Sham, Phys. Rev. A **140**, 1133 (1965).
[25] ADF1999, E. J. Baerends, A. Bérces, and C. Bo *et al.*
[26] A. D. Becke, Phys. Rev. A **38**, 3098 (1988).
[27] J. P. Perdew, Phys. Rev. B **33**, 8822 (1986).
[28] M. E. Casida, in *Recent Advances in Density Functional Methods*, edited by D. P. Chong (World Scientific, Singapore, 1995), pp. 155–192.
[29] M. E. Casida, in *Theoretical and Computational Chemistry*, edited by J. M. Seminario (Elsevier Science, Amsterdam, 1995), pp. 391–439.
[30] E. K. U. Gross, J. F. Dobson, and M. Petersilka, in *Topics in Current Chemistry*, edited by R. F. Nalewalski (Springer, New York, 1996), pp. 81–172.
[31] F. Salama, C. Joblin, and L. J. Allamandola, Planet. Space Sci. **43**, 1165 (1995).
[32] M. E. Casida, K. C. Casida, and D. R. Salahub, Int. J. Quantum Chem. **70**, 933 (1998).
[33] S. J. A. van Gisbergen, A. Rosa, G. Ricciardi, and E. J. Baerends, J. Chem. Phys. **111**, 2499 (1999).
[34] N. C. Handy and D. J. Tozer, J. Comput. Chem. **20**, 106 (1999).
[35] R. H. Judge, A. A Korale, J. J. York, D.-L. Joo, D. J. Clouthier, and D. C. Moule, J. Chem. Phys. **103**, 5343 (1995).
[36] M. E. Casida, C. Jamorski, K. C. Casida, and D. R. Salahub, J. Chem. Phys. **108**, 4439 (1998).
[37] R. van Leeuwen and E. J. Baerends, Phys. Rev. A **49**, 2421 (1994).
[38] Z.-L. Cai and J. R. Reimers, J. Chem. Phys. **112**, 527 (2000).